

Crustal Softening at Propagating Rift Tips, East Africa

F. Kolawole^{1,2}, R. Ajala¹

¹Lamont-Doherty Earth Observatory of Columbia University, Palisades, New York, 10964, United States

²Department of Earth and Environmental Sciences, Columbia University, New York, 10027, United States

Correspondence to: Folarin Kolawole (fola@ldeo.columbia.edu)

Abstract

We investigate the upper-crustal structure of the Rukwa-Tanganyika Rift Zone, East Africa, where earthquakes anomalously cluster at the northwestern tip of the Rukwa Rift, the eastern tip of the Mweru-Wantipa Rift, and along the Tanganyika Rift axis. The current is interacting with the Rukwa and Mweru-Wantipa rift tips host distributed faulting in exposed basement with little sedimentation. Here, we, manifested by prominent fault scarps and seismicity across the rift interaction zones. We invert earthquake P and S travel times to produce three-dimensional upper-crustal velocity models for the region, and perform seismicity cluster analysis to understand strain accommodation at rift interaction zones and the propagating rift tips. The resulting models reveal the occurrence of anomalously high Vp/Vs ratios that extend from the surface down to ca. 10 km at the tip zones of the upper-crust beneath the Rukwa and Mweru-Wantipa rifts. The spatial association of distributed faulting, upper-crustal seismicity, and thermal anomalies rift tips — regions with the basement exposures and sparse rift sedimentation. We detect distinct earthquake families within the deeper clusters which exhibit an upward linear temporal evolution pattern that suggests triggering by upward fluid migration and creep failure. A spatial transition from proximal tip zones dominated by thinned crust and through-going crustal and upper-mantle seismicity to distal tip zones with thick crust and dominantly upper-crustal seismicity indicate an along-axis variation in the controls on rift tip deformation. Overall, the collocation of basement faulting, crustal and upper mantle seismicity, and upper-crustal high Vp/Vs ratios suggest a mechanically weakened crust below the rift tips' flexural zone. We propose an ongoing strain localization and crustal softening at the rift tips that is at the rift tips, likely accommodated by brittle damage from crustal bending strain, and potentially compounded by and thermomechanical alteration by ascending fluids (mantle-sourced volatiles, and hydrothermal weakening. This setting represents a precursory phase that may initiate unilateral fluids). These findings provide new insights into the mechanics of continental rift tip propagation, linkage, and coalescence — a necessary ingredient for initiating a continental break-up axes.

1 Introduction

The mechanism of segmentation and lateral propagation and linkage of continental rifts, first introduced by Bosworth (1985), has received significant attention from the scientific community as they influence the structure and temporal progression of the evolving break-up axis (e.g., Ebinger et al., 1989, 1999; Nelson et al., 1992; Acocella, 1999; Aanyu and Koehn, 2011;

Allken et al., 2012; Corti, 2004; Zwaan et al., 2016; Neuharth et al., 2021; Kolawole et al., 2021a; Brune et al., 2023). Previous studies have established that continental rift systems grow by initial nucleation of isolated segments that propagate laterally, interact, link up, and coalesce to form longer composite rift basins with a continuous rift floor. Prior to linkage, the propagating rift segments are separated by an ‘unrifted’ basementcrustal block, and the lateral propagation of the rift deformation into the intervening block is essential to advance the rift system towards break-up (e.g., Nelson et al., 1992; Kolawole et al., 2021a; Brune et al., 2023).

In regions of active tectonic extension, inelastic deformation manifests by tectonic and magmatic deformation of the crystalline crust and its overlying sedimentary sequences in the rift basins (e.g., Brune et al., 2023; Pérez-Gussinyé et al., 2023). However, in magma-poor (i.e., non-volcanic) active rift settings, tectonic deformation in continental rifts is commonly accommodated by widespread brittle deformation of the crust through faulting and fracturing and accompanied by earthquakes (e.g., Muirhead et al., 2019; Kolawole et al., 2017, 2018; Gaherty et al., 2019; Zheng et al., 2020; Stevens et al., 2021). Nevertheless, little is known of how this deformation is transferred onto the propagating rift tips, and long-standing questions remain on how the earth’s crystalline crust accommodates and localizes tectonic strain during continental rift propagation.

HereIn this study, we utilizeuse recently acquired seismic data to explore the upper crustal structure of the Rukwa-Tanganyika Rift Zone (Fig. 1a), an active non-volcanic rift zone along the East African Rift System, where previous studies have suggested a thick, strong-~~cool~~ lithosphere (Craig et al., 2011; Foster and Jackson, 1998; Yang and Chen, 2010; Hodgson et al., 2017; Lavayssière et al., 2019) and ongoing unilateral propagation of the ~~rift tips~~Rukwa Rift tip (Kolawole et al., ~~2021~~2021a). A previous study (Hodgson et al., 2017) utilized the receiver function technique to map the spatial distribution of crustal-averaged Vp/Vs ratios but lacked constraints on the shallowest structure. Our results provide insight into the fundamental mechanism of strain distribution and localization along actively propagating rift segments. Ultimately, the approach may advance our understanding of how incipient divergent plate boundaries mature within active continental environments.

2 The Rukwa-Tanganyika Rift Zone

2.1 Pre-Rift Crystalline Basement

The crystalline crust of the Rukwa-Tanganyika Rift Zone (Fig. 1a) is mainly composed of metamorphic and igneous rocks of the Paleoproterozoic (1.85–1.95 Ga) Ubendian mobile belt (Fig. 1b), flanked by Archean crystalline rocks of the Bangweulu and Tanzania cratons and their overlying Neoproterozoic sedimentary sequences to the southwest and northeast respectively (Fig. 1b). The Ubendian Belt consists of several amalgamated NW-trending terranes defining the orogenic belt that accommodated the Paleoproterozoic collision events (2.025–2.1 Ga) between the Tanzania Craton and the Bangweulu Block. The terranes, comprising Ufipa, Katuma, Wakole, Lupa, Mbozi, Ubende, and Upangwa (Fig. 1b; Daly, 1988; Lenoir et al., 1994), are now exhumed due to long-term erosion and are bounded by steeply-dipping, ductile, amphibolite facies, strike-slip shear zones (Fig. 1b; Daly, 1988; Lenoir et al., 1994; Theunissen et al., 1996; Kolawole et al., 2018, 2021b; Lemna et al., 2019; Heilman et al., 2019; Ganbat et al., 2021). Their associated ductile fabrics are suggested to have influenced the

62 development of post-Precambrian rift basins in the region (Wheeler and Karson, 1994; Theunissen et al., 1996; Klerkx et al.,
63 1998; Boven et al., 1999; Heilman et al., 2019; Lemna et al., 2019; Kolawole et al., 2018, 2021a,b).

64 2.2 Phanerozoic Rifting History

65 The Rukwa-Tanganyika Rift Zone is defined by a system of NNW-to-NW-trending overlapping rift segments, consisting of
66 the Tanganyika Rift, the Rukwa Rift to its southeast, and the ENE-trending Mweru-Wantipa Rift located just southwest of
67 ~~its~~Tanganyika's southernmost sub-basin (Fig. 1a-b). The rift zone records multiple phases of Phanerozoic tectonic
68 extension, with the first phase occurring in the Late Permian to Triassic, the second phase beginning in the Late Jurassic but
69 peaking in the Cretaceous, and the third phase initiating in the Late Oligocene and presently persisting (e.g., Delvaux, 1989,
70 Roberts et al., 2012). Although studies show that all the rift segments are currently active (e.g., Daly et al., 2020; Hodgson
71 et al., Lavyssiere et al., 2019; Heilman et al., 2019; Kolawole et al., 2021a), ~~not~~ all the ~~sub-basins do not~~ record the three phases
72 of Phanerozoic rifting (Delvaux, 1989; Morley et al., 1992, 1999; Muirhead et al., 2019; Shaban et al., 2023). ~~In~~Within the rift
73 zone, the Rukwa Rift, ~~where there exist is~~ the only basin with basement-penetrating boreholes/borehole logs to constrain seismic
74 reflection interpretation, producing detailed mapping of the lateral extents of the Mesozoic and Cenozoic syn-rift sequences
75 (Morley et al., 1992) and relationships with rift faulting patterns (Morley et al., 1992, 1999; Heilman et al., 2019; Kolawole
76 et al., 2021b). The distribution of the syn-rift deposits and faulting patterns show that the Rukwa Rift progressively elongated
77 northwestwards and southeastwards over the rift phases. Its polyphase extensional tectonic history (Morley et al., 1999;
78 Heilman et al., 2019; Kolawole et al., 2021b).

Formatted: Font color: Auto

Formatted: Font color: Auto

80
81
82
83
84
85
86
87
88
89
90
91
92
93
94
95
96
97
98
99
100
101
102
103
104
105
106
107
108
109
110
111
112
113
114
115
116
117
118
119
120
121
122
123
124
125
126
127

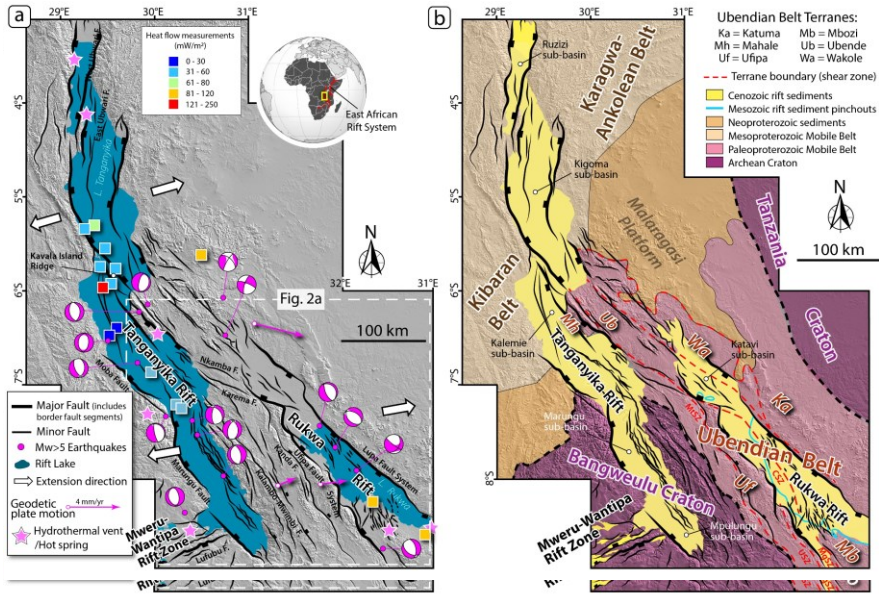


Figure 1. (a) Tectonic map of the Rukwa-Tanganyika Rift Zone showing the rift faults (Morley et al., 1999; Muirhead et al., 2019; Kolawole et al., 2021a). Focal mechanisms and epicenters of Mw > 5 earthquakes from National Earthquake Information Center (NEIC) catalog (1976–2018) obtained through the United States Geological Survey website (<https://earthquake.usgs.gov/earthquakes/search/>). Geodetic plate motion vectors are from Stamps et al. (2008). Regional extension directions are from Delvaux and Barth (2010) for the northern Tanganyika Rift and Lavayssi re et al. (2019) for the southern Tanganyika and Rukwa rift basins. Heat flow measurements and their locations are from Jones (2020). Sites of hot springs/hydrothermal vents are from Tiercelin et al. (1993), Lavayssi re et al. (2019), Jones (2020), and Mulaya et al. (2022). (b) Geological map of the region, showing the cratons, mobile belts, terranes of the Ubendian Belt and shear zones, and Cenozoic syn-rift sediments (modified after [Daly, 1988](#); Hanson, 2003; Delvaux et al., 2012; Kolawole et al., 2021a,b; Ganbat et al., 2021). **Ubendian Belt Terranes:** Ka - Katuma, Mb - Mbozi, Mh - Mahale, Ub - Ubende, Uf - Ufipa, Wa - Wakole. Exhumed Precambrian shear zones ([Delvaux et al., 2012](#); Heilman et al., 2019): CSZ, Chisi Shear Zone; MgSZ, Mughese Shear Zone; MtSZ: Mtose Shear Zone; USZ: Ufipa Shear Zone.

The Cretaceous rifting event included reactivated faulting, tectonic subsidence, and sedimentation in the Rukwa Rift and Luama Rift (e.g., Veatch, 1935; Delvaux, 1991; Roberts et al., 2012). Cenozoic rifting initiated the development of rift basins as segments of the "East African Rift System," featuring the reactivation of the Rukwa Rift and the development of the Tanganyika and the Mweru-Wantipa rift segments (e.g., Morley et al., 1999; Delvaux et al., 2001; Chorowicz, 2005; Daly et al., 2020). Crustal thickness across the rift zones range 31.6 – 42 km (Hodgson et al., 2017; Njinju et al., 2019) and lithosphere thickness 130 – 170 km (Njinju et al., 2019). The modern/contemporary regional extension direction/minimum compressive stress orientation is N74°E/074° in the northern Tanganyika Rift (Delvaux and Barth, 2010) and N80°E/080° in the southern

Formatted: Font color: Auto

Formatted: Font color: Auto

128 Tanganyika and Rukwa rifts (Lavyssière et al., 2019) (Fig. 1a). Although contemporary regional stress in the Mweru-
129 Wantipa Rift is unknown, the Mweru Rift, which is its southwestern continuation, is shown to have a regional minimum
130 compressive stress orientation of 118° (Delavaux & Barth, 2010).
131

132 2.3 Rift Faulting and Seismicity Patterns

133 The Tanganyika Rift basin is bounded by a system of large border faults that alternate polarity along-trend of the basin (Versfelt
134 and Rosendahl, 1989) and include the Marungu Fault, the Kavala Island Ridge Faults, the West and East Ubwari Faults, and
135 the Moba Fault (Fig. 1a), whereas the large graben of the Rukwa Rift basin is bounded by laterally continuous border fault
136 systems of the Lupa Fault to the northeast and Ufipa Fault to the southwest (Heilman et al., 2019). The Ufipa Horst represents
137 the intervening basement block between the southern Tanganyika Rift and the Rukwa Rift and is accommodating active
138 deformation as evidenced by the ca. 100-km long scarps of the Kanda and Kalambo-Mwimbi Faults (Fig. 1a; Delvaux et al.,
139 2012; Kolawole et al., 2021). Moreover, two prominent fault scarps extend westward WNW from the Rukwa Rift tip across a
140 basement region to the eastern margins of the central Tanganyika Rift (Nkamba and Karema Faults; Fig. 1a). The To the
141 southwest, the deformation zone of the Mweru-Wantipa Rift hosts a ca. 50-km-wide parallel fault cluster that defines its
142 southeastern margin within which the Lufuba Fault appears to have the greatest escarpment height (Fig. 1a).

143 The entire Rukwa-Tanganyika Rift Zone records widespread seismicity (Figs. 2a, c–d) that extends beyond 42 km depth,
144 indicating that the seismogenic layer of the rift includes the uppermost mantle (Fig. 2c–e; Lavyssière et al., 2019). The events
145 define clusters with focal mechanism solutions that suggest steep, deep-rooting, large normal faults (Lavyssière et al., 2019),
146 and highlight localized active crustal deformation zones beneath Tanganyika Rift, Rukwa Rift, the Ufipa Horst, and the
147 Mweru-Wantipa Rift (Fig. 1a). Across the rift zone, the earthquakes commonly initiate at the middle crust and extend
148 down into the lower crust, except, however, beneath the northwestern tip of the Rukwa Rift (Katavi sub-basin; Figs. 2a, 2d)
149 where the earthquakes primarily localized within occur in both the upper crust and upper mantle (Lavyssière et al., 2019).
150 More interestingly, the axis of the Rukwa Rift has sparse seismicity. Seismicity clusters at the Rukwa Rift tip extend beyond
151 the margins of the basin sediments, continuing outboard into the regions of the exposed pre-rift basement (Figs. 2a and 2d). In
152 the southern Tanganyika Rift, earthquakes mostly cluster within and along the rift axis and extend along most of the rift length
153 (Figs. 2a and 2c). Previous seismic receiver function and crustal anisotropy studies show evidence indicating the presence of
154 partial melt/volatiles in the lower crust (Hodgson et al., 2017; Ajala et al., 2024), and demonstrate how lower crustal fluids
155 promote strain localization (Ajala et al., 2024). Heat flow measurements in the rift zone show thermal anomalies in the central
156 Tanganyika Rift (<30 to 250 mW/m²), the south-central region of the Rukwa Rift (81 – 120 mW/m²), and within the basement
157 region ahead of the northwestern tip of the Rukwa Rift (81 – 120 mW/m²) (Fig. 1a; Jones, 2020). The thermal anomaly north
158 of the Rukwa Rift tip occurs near NW-trending fault splays and Mw>5 earthquake epicenters within the basement region.
159 Furthermore, hydrothermal vent and hot spring locations coincide with the border fault zones of the Tanganyika Rift and the
160 south-central part of the Rukwa Rift (Fig. 1a; Tiercelin et al., 1993; Lavyssière et al., 2019; Jones, 2020).

Formatted: Font color: Auto

Formatted: Border: Top: (No border), Bottom: (No border),
Left: (No border), Right: (No border), Between : (No border)

Formatted: Font color: Auto

Formatted: Font color: Auto

Formatted: Font color: Auto

Formatted: Font color: Auto

Formatted: Font color: Auto

Formatted: Font color: Auto

Formatted: Font color: Auto

Formatted: Font color: Auto

Formatted: Font color: Auto

Formatted: Font color: Auto

Formatted: Font color: Auto

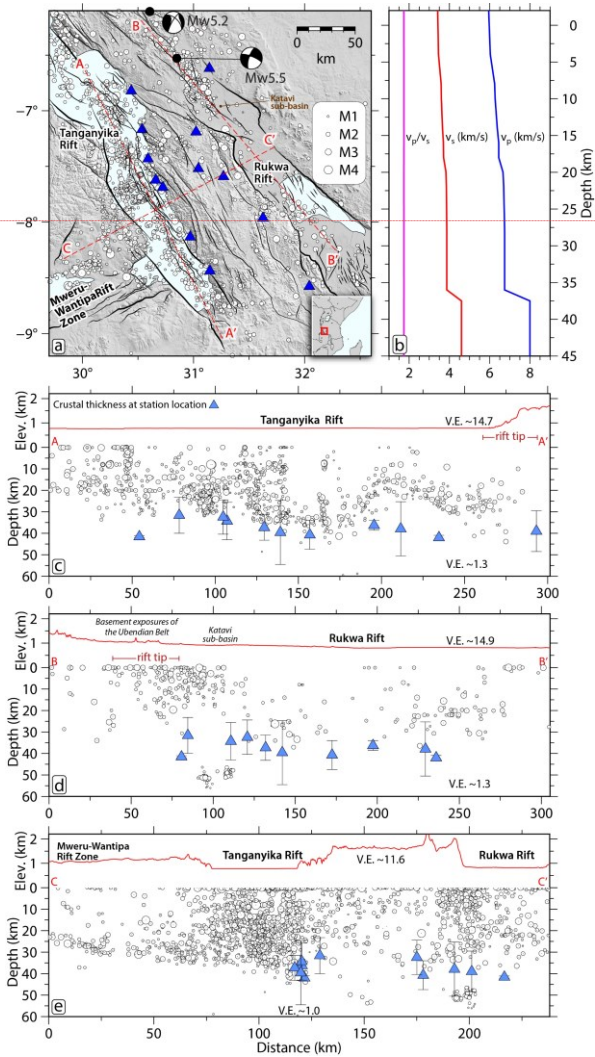
Formatted: Font color: Auto

Formatted: Font: Georgia, 11 pt, Font color: Auto,
Superscript

Formatted: Font color: Auto

Formatted: Font: Bold, Font color: Auto

161
162
163
164
165
166
167
168
169
170
171
172
173
174
175
176
177
178
179
180
181
182
183
184
185
186



Formatted: Font: 10 pt, Font color: Auto
Formatted: Space After: 12 pt

187

188 **Figure 2** (a) Map of the southern Tanganyika and Rukwa rift zone showing the local seismicity (white circles, from TANGA14 array
 189 network ZV, Lavayssière et al., 2019) scaled by magnitude. The black dots represent events used in the inversion. Previously deployed
 190 broadband seismometers are the blue triangles. Black lines are faults; the thicker black lines highlight border faults. Red dashed lines are
 191 locations of seismicity profiles in e-e'. Inset map shows the relative location in East Africa. (b) Starting model used in the seismic tomographic
 192 inversion (from Lavayssière et al., 2019). (c-e) Elevation and depth profiles showing projected seismicity from Lavayssière et al. (2019)
 193 and estimated Moho depths from Hodgson et al. (2017) along and across the rifts. Profiles A-A' and B-B' only show earthquakes within 25
 194 km.

195

196 **2.4 Active Deformation Across the Rift ~~Overlap~~ Interaction Zones**

197 At a regional scale, the Rukwa and Tanganyika rift basins are separated by an elevated region of pre-rift basement with
 198 widespread exposures of Precambrian metamorphic rocks (Figs. 1a-b; Kolawole et al., 2021a). This elevated region of rift
 199 overlap, described as includes the Ufipa Horst to its south, and the region between the northern tip of the Rukwa and the eastern
 200 flank of the central Tanganyika Rift to its north. In a geodynamic context, the geometry of the overlap region defines an
 201 overlapping parallel-to-oblique 'rift interaction zone' (Kolawole et al., 2021, 2021a) and is characterized by historical
 202 seismicity and active faults that deform the modern surface (Delvaux et al., 2001; Lavayssière et al., 2019; Kolawole et al.,
 203 2021a). The faults include the WNW-trending Karema and Nkamba faults, which splay westwards from the Rukwa Rift tip
 204 (Fig. 1a; Fernandez-Alonso et al., 2001; Kolawole et al., 2021a), and NW-trending faults that extend northwards towards the
 205 margin of the northern Tanganyika Rift (Kolawole et al., 2021a). The longitudinal surface relief morphology of the southern
 206 Tanganyika Rift shows a significantly steeper gradient than that of the Rukwa Rift tip ('rift tip' in Fig. 2c versus 2d). Overall,
 207 the current stage of evolution of the rift interaction zone based on the relief profile, stream flow patterns, and drainage
 208 morphologies is inferred to be partially breached (Kolawole et al., 2021a). The To the southwest, the Mweru-Wantipa Rift
 209 extends eastward and appears to be hard-linked with the border fault of the western flank of the southern tip of the Tanganyika
 210 Rift. The region between the two rifts defines an overlapping orthogonal rift interaction zone, and the continuation of Lake
 211 Tanganyika into the Mweru-Wantipa Basin and the apparent coalescence of the rift floors of the two basins suggest a breached
 212 rift interaction zone between them (Kolawole et al., 2021a).

213 **3 Body-Wave Tomography**

214

Formatted: Font color: Auto

Formatted: Font color: Auto

Formatted: Font color: Auto

Formatted: Font color: Auto

Formatted: Font color: Auto

Formatted: Font color: Auto

Formatted: Font color: Auto

Formatted: Border: Top: (No border), Bottom: (No border), Left: (No border), Right: (No border), Between: (No border)

Formatted: Font color: Auto

Formatted: Font color: Auto

Formatted: Font color: Auto

Formatted: Font color: Auto

Formatted: Font color: Auto

Formatted: Font: Not Bold, Font color: Auto

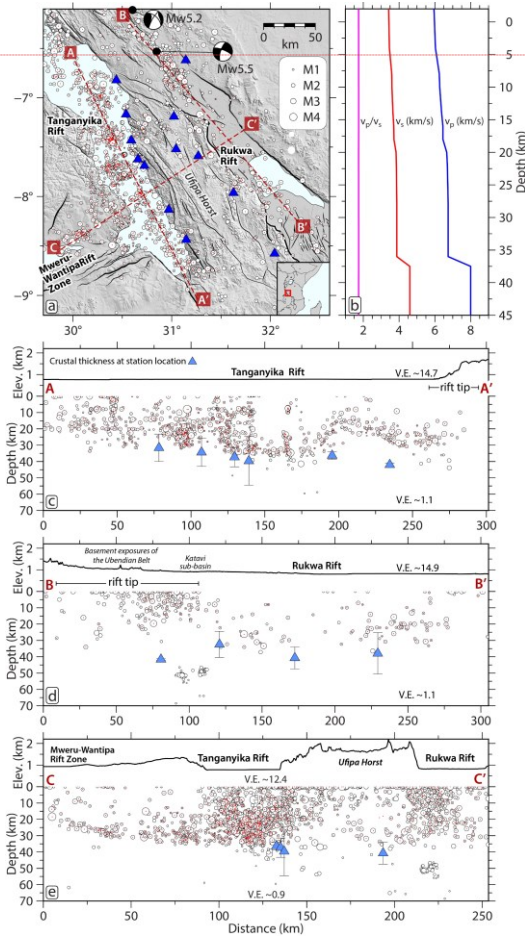


Figure 2. (a) Map of the southern Tanganyika and Rukwa rift zone showing the local seismicity (white circles; from TANGA14 array – network ZV, Lavayssière et al., 2019) scaled by magnitude. The red dots represent events used in the inversion. Blue triangles represent the locations of the TANGA14 broadband seismometers; Black lines are faults; the thicker black lines highlight border faults; Red dashed lines are locations of seismicity profiles in c-e. Inset map shows the relative location in East Africa. (b) Starting model used in the seismic tomographic inversion (from Lavayssière et al., 2019). (c - e) Elevation and depth profiles showing projected seismicity (from Lavayssière et al., 2019) and estimated Moho depths (from Hodgson et al., 2017) along and across the rifts. Cross-sectional profiles A-A' and B-B' only show earthquakes within 25 km on both sides of the cross-section traces, and all Moho depth plots are projected from stations located within 50 km of the profiles.

Formatted: Font: 10 pt, Font color: Auto

Formatted: Space After: 12 pt

Formatted: Font color: Auto

Formatted: Font color: Auto

Formatted: Font color: Auto

Formatted: Font color: Auto

Formatted: Font color: Auto

244
245
246
247
248
249
250
251
252
253
254
255
256
257
258
259
260
261
262
263
264
265
266
267
268

269
270

3 Data and Methods

3.1 Seismic Data

We focus on waveform data recorded by the TANGA14 array, comprising 13 broadband seismographs deployed along the Ufipa Plateau for 15 months from June 2014 through September 2015 (Fig. 2a; Hodgson et al., 2017). Using the origin times from the local earthquake catalog developed by Lavayssière et al. (2019) comprising 2213 events (Fig. 2a), we download the associated waveforms using the facilities of the EarthScope Consortium. The waveforms were then filtered with a Butterworth filter to accentuate the earthquake signal in the frequency band used in Lavayssière et al. (2019): 2 – 15 Hz. ~~First arrival~~Arrival times for both P and S waves were manually picked on filtered seismograms resulting in 3187 P times from 1277 earthquakes (resp. 3121 S times from 1261 earthquakes). We only made the travel time picks when the phases were clear and impulsive. We do not record uncertainty in arrival times during picking, nor do we pick multiple times to estimate the data variance.

3.2 Crustal Imaging

3.2.1 Backprojection Tomography

Using our manually picked P and S arrival times, we develop 3D P and S velocity models for the Tanganyika-Rukwa region via nonlinear back-projection travel time inversion (Hole, 1992; Hole et al., 2000). ~~Our preferred initial velocity model for the study area is, we use the 4D1-D P and S velocity model developed by Lavayssière et al. (2019)-) as our initial velocity model.~~ We parameterize the model space using a fixed 5 km grid spacing with dimensions of 425 km x 435 km x 50 km. The bottom right corner of the model is 29.1651° E and -9.6764° S and extends from 7 km above sea level to 43 km depth. Therefore, we use the actual station elevations without needing static corrections. The travel time predictions in the model are calculated using a finite-difference solution for the Eikonal equation (Vidale, 1990), which allows travel times to be computed for all grid points in the model. Ray paths are then simultaneously traced for any number of source-receiver pairs using the gradient of the travel time field. Due to the reciprocity in the travel time computation, we treat the receivers as sources, thus, requiring only 13 forward computations in each iteration. Following the forward calculation, we iteratively update the models, k , at each grid point, j , as follows:

$$u_{k+1}^j = u_k^j + \delta u_{k,j}^j \quad \Theta(1)$$

where the slowness perturbations, δu , are calculated using simple back-projection as the average of the neighborhood ray paths, i.e.,

Formatted: Font color: Auto

Formatted: Border: Top: (No border), Bottom: (No border), Left: (No border), Right: (No border), Between : (No border)

Formatted: Font color: Auto

Formatted: Font color: Auto

Formatted: Font color: Auto

Formatted: Font color: Auto

Formatted: Border: Top: (No border), Bottom: (No border), Left: (No border), Right: (No border), Between : (No border)

Formatted: Font color: Auto

Formatted: Font color: Auto

Formatted: Border: Top: (No border), Bottom: (No border), Left: (No border), Right: (No border), Between : (No border)

Formatted: Font: Cambria Math, 10 pt

Formatted Table

$$\delta u_k^j = \frac{1}{N} \sum_{\text{cells}} \sum_{\text{rays}} \frac{\delta t_{\text{ray}}}{l_{\text{ray}}}, \quad (2)$$

Formatted: Font: Cambria Math, 10 pt

Formatted Table

with δt and l being the associated traveltimes residual and raypath length for the associated ray. We further smooth the perturbations once they are determined for all grid points in the model using a 3D moving average filter to control the spatial resolution and stabilize the inversion. This procedure is like higher-order Tikhonov regularization in the least squares nonlinear inversion. We gradually reduce the size of the smoothing dimension after every five iterations to increase the spatial resolution of the model. The final smoothing size of our model from the 26th iteration is $5 \times 5 \times 3$ grid points. ~~Subsequent iterations do not have substantially lower misfits but become contaminated by noise (Fig. S1).~~ Finally, the Vp/Vs ratio is obtained by dividing the P and S velocity models.

3.3.2.2 Model Reliability Assessment

To assess the model uncertainty, we employ a combination of ray coverage maps, classical checkerboard reconstruction tests, a custom synthetic model reconstruction test, ~~(targeted resolution test, e.g., Saicid et al., 2024),~~ and real data inversion using different starting models to determine areas of the model reliable enough for interpretation (Figs. 3 – 5 and S2 – S18). We generate the checkerboard models by adding 3D sinusoid functions to the initial velocity model (Fig. 2b) using similar magnitudes in the amplitudes of the real, inverted model (Fig. S3). The observed travel time dataset is computed in the checkerboard model and then inverted using the unperturbed starting model. We do not add noise to the synthetic datasets. We also test different sizes of the anomalies (Figs. S4 – S15). Based on the results from the artificial reconstructions, we define a polygon (e.g., Figs. S16 and S3) in the model space where the model parameters are reasonably resolved ~~and note that the checkerboard anomalies are accurately recovered in areas of the polygon with zero or sparse ray coverage.~~ Also, we developed and inverted a custom synthetic model (Figs. S16 and S17) based on the vital features we interpret in our final preferred model (Fig. S3) at the edge of the polygon where ray coverage is sparse or lacking (Fig. S2).

Formatted: Font color: Auto

Formatted: Font color: Auto

Formatted: Border: Top: (No border), Bottom: (No border), Left: (No border), Right: (No border), Between : (No border)

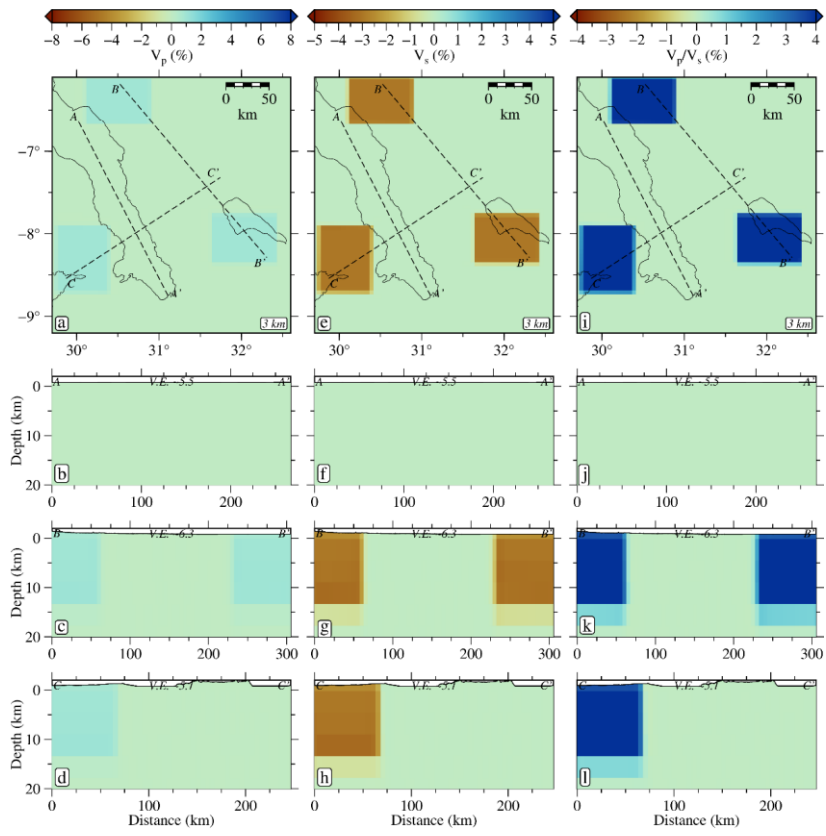


Figure 3. True custom-synthetic model generated by perturbing the P (1% increase) and S (3% decrease) velocity models to generate three V_p/V_s (-4% increase) anomalies. (a) 3-km depth slice through the P-wave velocity model. Dashed black lines show the profile locations in b-d. (b-d) Profiles of the P-wave velocity model. (e-h) Same as a-d but for the S-wave velocity model. (i-l) Same as a-d but for the V_p/V_s ratios.

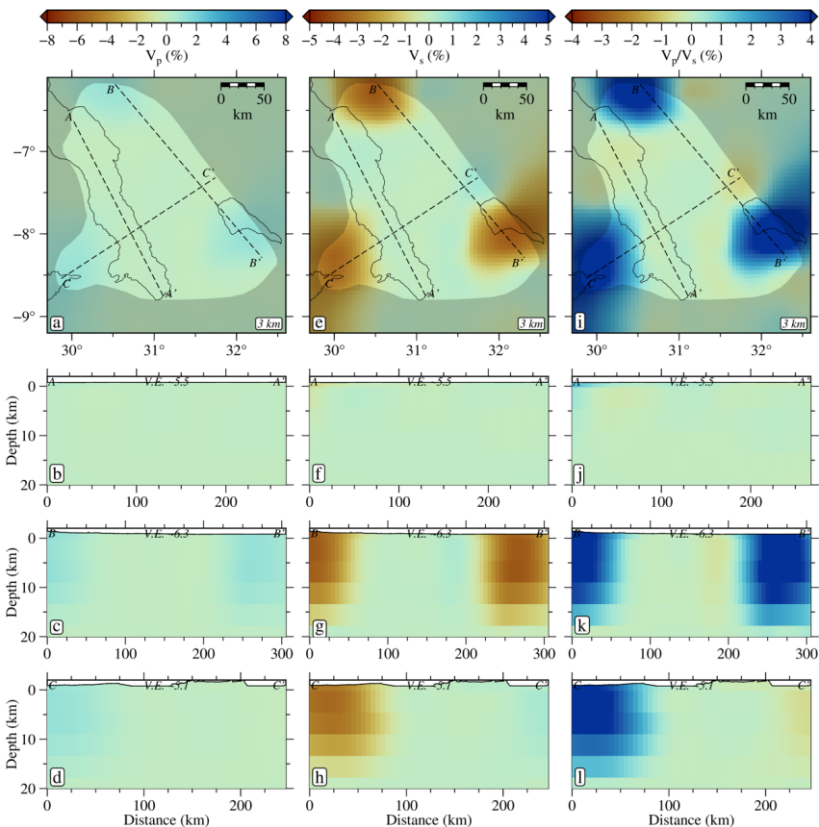


Figure 4. Recovered custom synthetic model from Fig. 3. (a) 3 km depth slice through the P-wave velocity model. Dashed black lines show the profile locations in b-d. Unreliable areas of the model are lightly grayed-out. (b - d) Profiles of the P-wave velocity model. (e - h) Same as a-d but for the S-wave velocity model. (i - l) Same as a-d but for the V_p/V_s ratios.

The synthetic model comprises three high V_p/V_s (~4 % increase) anomalies generated by perturbing the P (1 % increase) and S (3 % decrease) velocity model and extending from 2 km above zero to 13 km depth in the model space, with the following horizontal dimensions: 80 by 60 km at the north, 80 by 60 km at the southeast, and 65 by 85 km at the southwest. The inversion results show good recovery of the anomalies with some smearing outside our predefined polygon (Fig. 4S17). To further assess the reliability of these features in the real model (Fig. 53), we perform two other inversions of the real data using two different

389 3D initial velocity models from Celli et al. (2020) and van Herwaarden et al. (2023). A comparison of the results of all three
 390 starting models (Figs. S16—S18—S20) shows that the Vp/Vs anomalies are robust.

391 **3.4 Preferred Inversion Result**

392 **3.3 Seismicity Cluster Analysis**

393 Visual inspection of the seismicity (Fig. 2) shows apparent spatial clusters. However, we must perform a spatiotemporal
 394 seismicity clustering analysis to determine which earthquakes are also close in time (Fig. S21). Although a complete statistical
 395 study of the earthquake catalog is beyond the scope of the current research, we perform a simple clustering analysis (Fig. S22)
 396 to highlight potential earthquake groups that could indicate fluid activity at the rift tips. First, we attempt catalog declustering
 397 to remove any aftershock sequences using the approach of Reasenberg (1985) as implemented in the CLUSTER2000 program.
 398 However, no significant aftershock sequences were found, with most aftershock clusters totaling 17 containing only two events
 399 (Ajala & Kolawole, 2023). This is despite the earthquake frequency distribution (Fig. S23e) showing a decreasing amount of
 400 seismicity through time that would seemingly indicate the presence of aftershock sequences. The lack of correlation between
 401 the data availability periods when the seismic stations were operational (Fig. S23a) and the seismicity frequency (Fig. S23e)
 402 shows that there was indeed increased seismic activity during the earlier deployment times, particularly in August 2014. An
 403 enhanced earthquake catalog with a lower magnitude of completeness may be required in the region for declustering.
 404 Therefore, we decided to use the entire catalog as is in the clustering analysis. We analyze the earthquake catalog for clusters
 405 using the algorithm of Zaliapin et al. (2008) and Zaliapin & Ben-Zion (2013), as implemented by Goebel et al. (2019). For
 406 each event j in the catalog, except for the earliest one, we find the parent event, which is an earlier event, defined using the
 407 smallest nearest-neighbor distance η_{ij} computed to all the other events i and defined as

$$398 \eta_{ij} = \begin{cases} t_{ij} r_{ij}^{d_f} 10^{-b m_i}, & t_{ij} > 0 \\ \infty, & t_{ij} \leq 0 \end{cases} \quad (3)$$

408 where t_{ij} is the time separation in years, r_{ij} is the Haversine distance between the earthquake pairs epicenters, d_f is the fractal
 409 dimension of the epicenters assumed to be 1.6 (Zaliapin et al., 2008), b is the Gutenberg-Richter b-value set to 1, and m_i is
 410 the magnitude of the potential parent event i . To separate the nearest-neighbor distances into space R_{ij} and time T_{ij}
 411 components, we use the following relations.

$$412 T_{ij} = t_{ij} 10^{-q b m_i}, \quad (4)$$

$$413 R_{ij} = r_{ij}^{d_f} 10^{-(1-q) m_i}, \quad (5)$$

414 where we assume an interpolation factor q of 0.5.

415 Finally, to split the catalog into background and cluster events, we estimate a separation threshold η_0 using the average of
 416 estimates of the 1st percentile of nearest-neighbor distances computed from 100 randomized catalogs with a similar range of
 417 space-time-magnitude parameters but with a Poissonian distribution representative of background seismicity (Fig. S22). At
 418
 419

420 the estimated η_0 , we see the probability distribution of the nearest-neighbor distances deviate from the Weibull probability
421 distribution known to represent Poisson background seismicity (Fig. S22c; Zaliapin & Ben-Zion, 2013). Event pairs with
422 nearest-neighbor distances less than η_0 that have similar parents are then recursively grouped to generate the clustered catalog
423 (Figs. 4, S23b – d, and S24). For clusters at the Rukwa rift tip, we compute the normalized cross-correlation coefficients of
424 the vertical component of the waveforms of events relative to the waveform of the parent event (Figs. 4g and h). We note that
425 the lack of uncertainties in the earthquake catalog (Lavayssière et al., 2019) and relative earthquake locations may introduce
426 spatiotemporal errors in the above analysis. In presenting our results, we use the time-magnitude plots as a guide to help
427 distinguish between the mechanisms of the two swarms as either slow slip (creep) or fluid flow (Roland & McGuire, 2009).
428

429 **4 Results**

430 **4.1 Crustal Seismic Velocity Models of the Tanganyika-Rukwa Rift Zone**

431 We present ~~our preferred~~the velocity models as perturbations (Fig. 5j) relative to the starting models used in the inversion
432 (Fig. 2b). The 5 km model grid spacing makes our selection of the 3 km depth maps (Figs. 5a–3c, ~~and~~3i, 4c, 4i, 5a, 5c, 5j)
433 representative of the average uppermost crustal structure of the model in the region, as can be verified in the cross-sectional
434 profiles of ~~Fig. 3~~Figure 5. The overall distribution of upper crustal velocities generally reflects the near-surface geology, which
435 serves as a primary constraint for assessing the quality of the models. Our results show that ~~slower~~lower Vp and Vs are
436 collocated with the sedimentary basins of the southern Tanganyika and Rukwa rifts. Relatively lower velocities continue along
437 a narrow ESE-trending zone from the Tanganyika Rift to the northern end of the Rukwa Rift, following the Nkamba and
438 Karema faults. The Ufipa Horst separating the Tanganyika and Rukwa rifts also shows localized zones of ~~Lower~~lower Vp,
439 collocated with areas of ~~pervasive~~prominent surface faulting (Fig. 5a3a). However, unlike the Vp distribution, the Ufipa Horst
440 is better defined in the Vs model, demonstrated by the relatively higher values and structural continuity (Figs. 5e3e and h).
441 Within the eastern section of the Mweru-Wantipa Rift and further east towards the southern Tanganyika Rift, we observe
442 moderate Vp anomalies collocated with moderate-to-low Vs anomalies (Figs. 5a3a – b, e – f). Overall, the rift flanks and zones
443 of widespread exposure of the pre-rift basement exhibit relatively higher Vp and Vs.

444 The Vp/Vs ratio map (Fig. 5j3j) and cross-sections (Figs. 5j3j – l) show zones of anomalously high values that are restricted
445 to upper-crustal depths, the most prominent of which are A1: an anomaly at the northwestern end of the Rukwa Rift, an area
446 dominated by basement exposures and distributed faulting, A2: a broad anomaly extending across the eastern end of the
447 Mweru-Wantipa Rift through the transfer zone into the Tanganyika Rift, and A3: an anomaly in the southeastern interior of
448 the Rukwa Rift, collocated with the Ufipa Fault and the intra-basement Chisi Shear Zone (Fig. 1b). These highest Vp/Vs
449 anomalies commonly continue downward to 10 km or deeper (Figs. 5k3k – l) but our investigation focuses on the upper crust.

450 **4.2 Spatiotemporal Clustering of Rift Tip Seismicity**

Formatted: Border: Top: (No border), Bottom: (No border),
Left: (No border), Right: (No border), Between : (No border)

Formatted: Font color: Auto

451 Our cluster analysis yielded 115 clusters, but we only retained clusters with a minimum of 5 events, resulting in a filtered
452 number of 18 clusters. The distribution of these clusters is shown as colored circles in map and cross-section views in Figures
453 4a–d and Figure S24 and as functions of latitude, longitude, and depth in Figures S23b – d. We identify clusters throughout
454 the crust and in the upper mantle, with most of the clusters occurring along the intra-rift faults within the Tanganyika Rift.
455 Some clusters are located at the tips of the Mweru-Wantipa and Rukwa rifts and on faults within the Ufipa Horst. Due to the
456 focus of the current study on investigating rift tip processes, we only discuss the detected seismicity clusters at the Rukwa Rift
457 tip, the three spatially clustered events occurring at 10 – 20 km depth at the Mweru-Wantipa Rift tip, and the absence of clean
458 waveform records for these events preclude further analysis on these clusters.

459 There are two main clusters at the Rukwa rift tip (Figs. 4a – d), both occurring in the upper mantle between 40 – 70 km depths.
460 The northern cluster comprises six events with local magnitudes between 0.67 and 1.35 that happened within a period of ~50
461 minutes on July 9, 2014 (Fig. 4e). In contrast, the southern cluster has 12 events with magnitudes between 1.2 and 2.8 that
462 occurred within a period of ~19 days in June 2015 (Fig. 4f). We note the high waveform similarity of the events as recorded
463 at nearby stations (Figs. 4g and h). In general, both clusters define a generally linear trend with the shallower events occurring
464 later, indicating a generally upward migration (Figs. 4c and d). Although the relative timing of the largest magnitude event in
465 a cluster is often used as a proxy for defining aftershock sequences, here in the southern cluster, the magnitudes of the events
466 are low and primarily similar. Furthermore, the seismicity distribution does not follow Omori’s decay law since our clustering
467 analysis would otherwise have detected it (Ajala & Kolawole, 2023).

469 **5 Discussion**

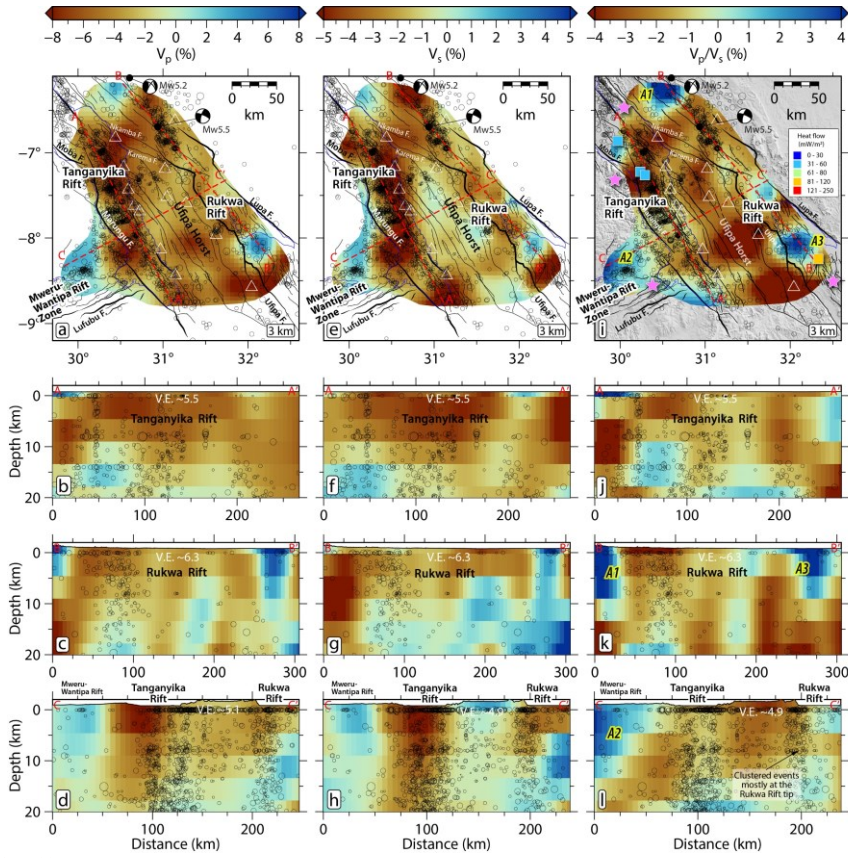
470 **Fault-related damage and distributed brittle 5.1 Crustal Softening in the Rukwa-Tanganika Rift Zone**

471 Brittle deformation in the crystalline crust often create, including fault- and folding-related damage, commonly creates zones
472 of decreased bulk crustal density regions, manifested as zones of anomalously low Vs and high Vp/Vs zones ratio (Allam et
473 al., 2014; Fang et al., 2019). Also Similarly, regions where brittle damage allows the hosts melts/volatiles, and/or upwelling of
474 hydrothermal fluids in the upper crust are associated with relatively higher Vp/Vs values (e.g., Chatterjee et al., 1985; Nakajima
475 et al., 2001; Hua et al., 2019). In active rift settings with absent surface volcanism, understanding the spatial distribution of
476 upper-crustal seismic velocities permits the identification of mechanically weakened zones where tectonic strain may be
477 preferentially localized. Delineating these near-surface structures will help to better understand how the crust accommodates
478 tectonic strain along actively propagating rift basins and predict ground motion amplification during large earthquakes (Ajala
479 and Persaud, 2021; e.g., Cormier and Spudich, 1984; Ajala and Persaud, 2021).

Formatted: Justified, Border: Top: (No border), Bottom: (No border), Left: (No border), Right: (No border), Between : (No border)

480
481
482

In the
Rukwa-



483
484
485
486
487
488

Tanganyika Rift Zone, two

489
490
491
492
493
494
495
496
497
498
499
500
501
502
503
504
505
506
507
508
509
510
511
512
513
514
515
516

Figure 5. Maps and profiles through the tomographic models showing the perturbations relative to the starting models in Fig. 2b. (a) 3 km depth slice through the P wave velocity model. Unreliable areas of the model are not shown. Dashed black lines show the profile locations in b-d. (b-d) Profiles of the P wave velocity model. (e-h) Same as a-d but for the S wave velocity model. (i-l) Same as a-d but for the Vp/Vs ratios. Absolute values of the model parameters are shown in Fig. S16. Note that the geothermal center near anomaly A1 is north of latitude 6°S which is outside of the map coverage (see Fig. 1a).

Formatted: Font color: Auto

Two of the three areas of the highest upper-crustal Vp/Vs ratios (A1 and A2) occur at rift tips where syn-rift sedimentary cover is thinnest, and basement exposures dominate the surface geology (Figs. 1b and 3i). These anomalies occur at or near geothermal anomalies (Fig. 1a) hot springs and high heat flow sites in Figs. 1a, 3i) and are collocated with earthquake clusters and distributed normal faults. The anomalous seismicity cluster at the tip indicates the focus of active brittle deformation of the crystalline crust in a region that is lacking well-developed rift basins. At the Rukwa Rift tip and further to the northwest, the faulting pattern is generally characterized by distributed faults/fault scarps that extend/continue outboard from the Rukwa Rift-border faults into the rift interaction zone (Fig. 1a). At the Mweru-Wantipa Rift tip, the rift faults appear to mainly cluster near the southern/southeastern rift margin. Thus, we interpret the occurrence of the high upper-crustal Vp/Vs anomalies at the modern rift tips to represent a localization zone of mechanically weakened crystalline crust.

517

518

519

520

521

522

523

524

525

526

527

528

529

530

531

532

533

534

535

536

537

538

539

540

541

542

543

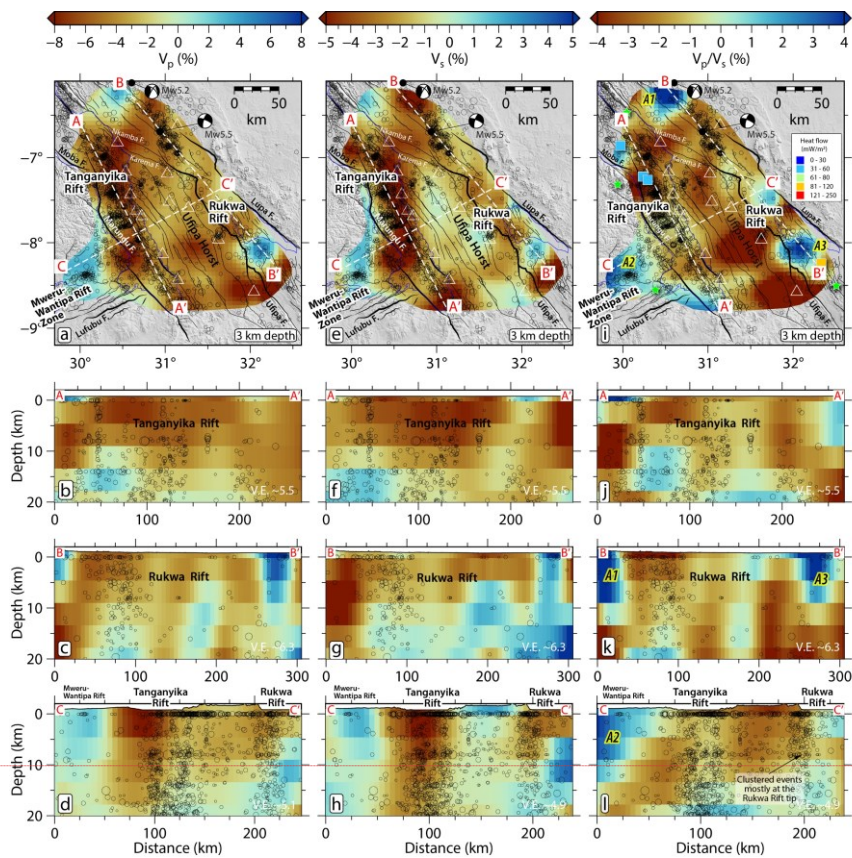


Figure 3. Maps and profiles through the tomographic models showing the perturbations relative to the starting models in Fig. 2b. (a) 3 km depth slice through the P wave velocity model. Unreliable areas of the model are not shown. Dashed black lines show the profile locations in b-d. (b-d) Profiles of the P wave velocity model. (e-h) Same as a-d but for the S wave velocity model. (i-l) Same as a-d but for the V_p/V_s ratios. Absolute values of the model parameters are shown in Fig. S16. Note that the geothermal center near anomaly A1 is north of latitude 6°S which is outside of the map coverage (see Fig. 1a).

Formatted: Font color: Auto

Localization

5.2 Mechanical Weakening of Rift Tips: The Roles of Bending Strain and Crustal Fluids

The development of mechanically weakened crust at active rift tips reflects a critical rift process facilitating the growth of relevant for understanding how continental rift systems rifts propagate. This is analogous to microfracture propagation driven by high-stress concentrations at the crack tips (e.g., Kranz, 1979; Olson, 2004). Similarly, relatively large stress concentrations between interacting microcrack tips (Kranz, 1979) agrees with interpretation of stress concentrations within rift interaction zones that separate propagating rift tips (Kolawole et al., 2023). Here, the The northwestern tip of the Rukwa Rift is characterized by geomorphic features and tectonic deformation patterns that suggest an ongoing northwestward propagation towards the central and northern Tanganyika Rift (Kolawole et al., 2021a). The earthquake clusters at the Rukwa and Mweru-Wantipa rift tips (Fig. 2a) indicate that tectonic stresses and elastic strain concentrations are focusing at on the rift tip zones. These The brittle deformation field that is manifested by these earthquakes are is likely induced by accommodating the bending stresses and the associated plastic strain along the rift tip's flexural margin (Fig. 6a). Several studies have demonstrated that crustal bending due to accumulated fault displacement, glacial unloading, thermal subsidence, or sediment load induced crustal subsidence can focus significant strain in the upper crust, leading to brittle failure of the crust (e.g., Goetze and Evans, 1979; Stein et al., 1979; Nunn, 1985). Here, long-term accrual of fault displacement and sediment loading on along the central hanging walls of the Lupa and Ufipa border faults causes crustal basement down-flexure in the rift axis basin and proximal sections of the rift tip, and contemporaneous crustal basement upwarping at the distal section of the rift tip (Fig. 6a). The upwarping of the basement crustal bending at the rift tips induces significant extensional strain in the upper part of the brittle lithosphere, which explains may explain the localized clusters prominent occurrence of earthquakes at the rift tips, best expressed at the northwestern tip zones of the Rukwa Rift (Figs. 2a, 2d). Thus, Since there is no data on the border fault displacements or basement depth variations from the rift axis into the areas of exposed basement ahead of the rift tip, we cannot provide a detailed analysis of how the changes in basement flexure imposes extensional vs contractional strain on the upper crust. Nevertheless, we suggest that damage clustering at the propagating rift tip is a relevant fundamental process that may facilitate mechanical weakening at the tips of active continental rifts.

In addition to bending strain-related earthquakes in the crust, the temporal and upward linear trends of low-magnitude seismicity migration in the upper mantle beneath the proximal rift tip in the Rukwa Rift tip (Figs. 4b-f) suggest fluid (volatiles) related earthquake triggering. We interpret that the northern cluster likely represents fluid-induced microseismic creep due to the fast migration velocity (>1 km/hr) (Fig. 4e), and the southern cluster likely indicates fluid flow due to the much slower linear migration velocity (Fig. 4f) (e.g., Zhang & Shearer, 2016). These results are further corroborated by the high waveform similarity of the events recorded at nearby stations (Figs. 4g and h; Raggiunti et al., 2023). In the Tanganyika Rift, the detected spatiotemporally clustered events extend up from the moho to the upper-crust (Fig. S24), and the events are primarily in the crust beneath the Mweru-Wantipa Rift tip (Fig. S24e). Although primarily hosted in the crust, we interpret that the detected clustering events in the Tanganyika and Mweru-Wantipa are likely also triggered by fluids, and that the fluids are potentially related to both mantle and hydrothermal sources. Thus, our cluster analysis results are consistent with previous studies that

suggest the presence of partial melt in the crust beneath Tanganyika Rift Zone (Hodgson et al., 2017; Lavaysseier et al., Ajala et al., 2024).

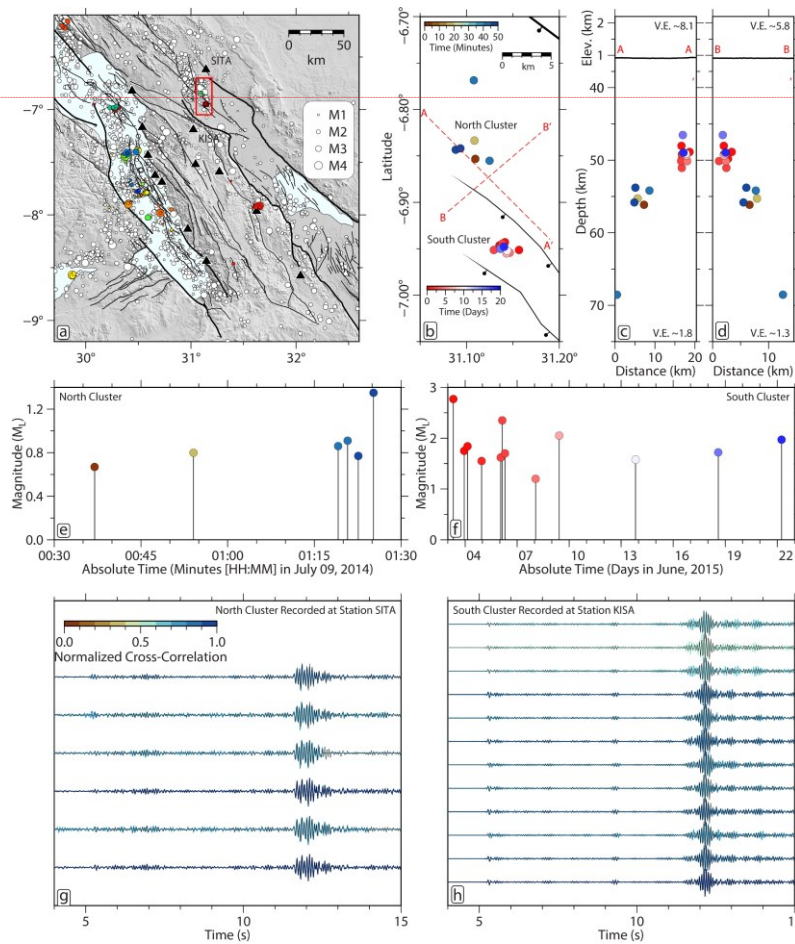


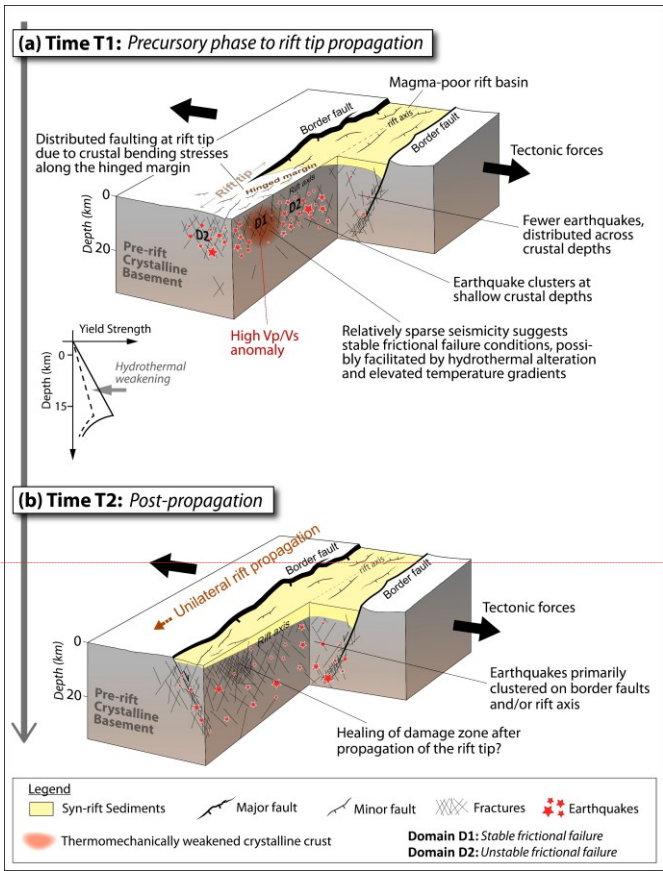
Figure However, we note that the seismicity clusters are not collocated with the high V_p/V_s ratio anomalies but occur near their margins (Figs. 5i). We interpret this to indicate a transition from one frictional stability domain to another within the upper crust. Fluid saturation and pressure may decrease the effective normal stresses on basement faults and fractures, leading to their failure. Nevertheless, the brittle failure may be aseismic or seismic depending on the lithology of the fault rocks (and

Formatted: Font: Not Bold

Formatted: Space Before: 12 pt, After: 12 pt, Line space 1.5 lines

601 ~~host rocks) and loading conditions~~4. Delineation of spatiotemporal seismicity clusters with a focus on the Rukwa rift tip swarms. (a)
602 ~~Map of the study area showing the broad seismicity and detected spatiotemporal clusters (colored circles). Red polygon indicates the frame~~
603 ~~for the clusters shown in panel b. (b) Zoom-in map of the two clusters at the Rukwa tip color-coded according to their occurrence in time~~
604 ~~relative to the parent event (i.e., first event) in each group. Red dashed lines are the locations of the cross-sectional profiles in panels c and~~
605 ~~d. (c) Rift-parallel, and (d) Rift-perpendicular profiles showing the projected clusters. (e) Magnitude-time plot for the northern cluster events.~~
606 ~~(f) Magnitude-time plot for the southern cluster events. (g) 2–15 Hz waveform records for the north cluster events recorded at station SITA~~
607 ~~highlighted in panel a. Each waveform is colored using the normalized cross-correlation coefficient computed by comparing the similarity~~
608 ~~of each waveform in the sequence to the waveform of the parent event. The parent event waveform is also plotted on all the waveforms as a~~
609 ~~black line for visual comparison. All traces have been time-shifted to maximize the correlation. The maximum cross-correlation value occurs~~
610 ~~for the first trace since it represents the autocorrelation (correlation of the parent waveform with itself). (h) Similar to panel g but for the~~
611 ~~southern cluster recorded at station KISA.~~
612
613

614 ~~The spatial relationship between large earthquake clustering and the velocity distribution in the upper crust may provide insight~~
615 ~~into how bulk rock alterations may influence seismicity and strain accommodation at the rift tips. The occurrence of geothermal~~
616 ~~anomalies in the vicinity of the high Vp/Vs ratio anomalies suggest that ascending fluids may be advecting heat into the upper~~
617 ~~crust. At both the Rukwa and Mweru-Wantipa Rift tips, we observe that the most prominent seismicity clustering occurs near~~
618 ~~the margins of the high Vp/Vs ratio upper-crustal anomalies, and not within the anomalies (Figs. 3i,k,l). We infer that this~~
619 ~~pattern indicates frictionally stable conditions promoting aseismic failure within the crustal blocks of high Vp/Vs ratio, and~~
620 ~~frictionally unstable conditions promoting seismic failure in their surrounding crust. The brittle failure of brittle discontinuities~~
621 ~~may be aseismic or seismic depending on confining stress, temperature, and compositional characteristics of the crust and the~~
622 ~~fault rocks they host (e.g., Blanpied et al., 1991; Carpenter et al., 2011; Kolawole et al., 2019). Given the same loading~~
623 ~~conditions around the rift tip, we infer tips, it is possible that pervasive compositional alteration (likely hydrothermal) significant~~
624 ~~fluid-rock alterations of the crust due to the migrating fluids within the areas of highest Vp/Vs could have created compositional~~
625 ~~variations that promote aseismic failure resulted in frictionally stable conditions within the zones of highest Vp/Vs ratios (D1~~
626 ~~in Fig. 6a) as opposed to their surrounding regions that are failing by seismogenic deformation (zone D2). The Vp/Vs anomaly~~



Within

Formatted: Font: Not Bold

Formatted: Space Before: 12 pt, After: 12 pt, Line spacing: 1.5 lines

659
660
661
662
663
664
665
666
667
668
669
670
671
672
673
674
675
676
677
678
679
680
681
682
683
684
685
686
687
688
689
690
691
692
693
694

~~Figure 6. (a – b) Cartoons showing the newly proposed model central regions of crustal strain accommodation during the unilateral propagation phase of an active continental rift tip as suggested by the results of this study.~~

~~A3 within the Rukwa Rift, the Vp/Vs anomaly A3 is collocated with an area of relatively less intra-rift fault occurrence (Fig. 5i). However, this anomaly but is in the hanging wall of the Ufipa border fault near a known geothermal anomaly (Jones, 2020). Since A3 is confined to <5 km depth (Fig. 5k), it may also likely represents represent a compositionally altered and mechanically weakened section of the border fault and its hanging wall block, similar to velocity anomalies observed near geothermal field of active rifts elsewhere (e.g., Hauksson and Unruh, 2007).~~

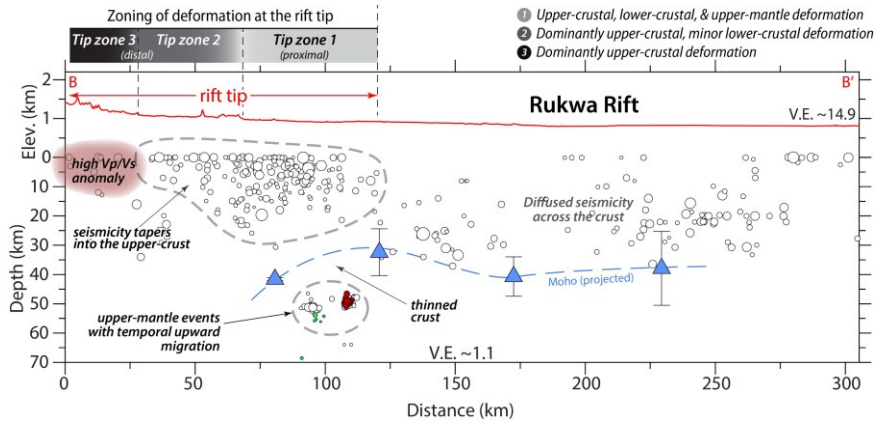
~~Although our results generally indicate active deformation at the propagating rift tips of the Rukwa and Mweru-Wantipa rifts, the relatively greater abundance of data at the Rukwa Rift tip permit a characterization of how the controls on the deformation may vary from the proximal rift tip zones to the distal tip zones. The depth distribution of seismicity and the detected spatiotemporal seismicity clusters, the along-rift variation of crustal thickness, and relative location of high Vp/Vs anomaly suggest that the proximal tip zones (tip zone 1) is dominated by upper-crustal, lower-crustal, and upper-mantle deformation (Fig. 5). However, the crust appears to thicken towards the distal tip zones (tip zones 2 to 3) and the seismicity patterns appear to become shallower and primarily focusing on the upper crust at tip zone 3 (Fig. 5). In general, we infer a through-going crustal deformation in the proximal rift tip zones controlled by crustal thinning and infiltration of volatiles into the crust with focused crustal bending strain (synclinal?), all of which transition into a dominantly upper-crustal deformation at the distal tip zones where bending strain (anticlinal) and fluid-rock alterations control the brittle deformation. Published models for rift linkage demonstrate that rift basins can propagate laterally and interact when in proximity (e.g., Allken et al., 2012; Corti, 2012; Molnar et al., 2019; Nelson et al., 1992; Zwaan et al., 2016; Zwaan and Schreurs, 2020; Neuharth et al., 2021; Kolawole et al., 2021a). Studies of natural rifts Models also show that inherited crustal mechanical barriers, non-optimal rift interaction zone geometry, or unfavorable tectonic stress distribution can stall lateral rift propagation (e.g., van Wijk and Blackman, 2005; Kolawole et al., 2022, 2023; Shaban et al., 2023). Numerical models show that the stalling of a laterally propagating rift tip creates a local tips may host stress concentration zones (van Wijk and Blackman, 2005; Le Pourhiet et al., 2018). Our study presents evidence from a natural rift for the first time, revealing localized the presence of crustal weakening at a laterally propagating continental rift tip, and in addition, shows how the weakening is likely controlled by a combination of crustal bending strain and fluids (ascending volatiles and migrating hydrothermal fluids). We propose a model for lateral rift~~

Formatted: Font: 10 pt

Formatted: Font: 10 pt

Formatted: Space Before: 0 pt, After: 0 pt, Line spacing Multiple 1.36 li

695 propagation whereby ~~the inception of progressive rift tip~~ propagation is marked by the development of localized brittle
 696 ~~damageweakened crust at the rift tip~~ (Time T1, Fig. 6a). ~~Subsequently, the weakened crust~~ which subsequently gives way
 697 to a lengthened rift basin (Time T2, Fig. 6b).



722 **Figure 5.** Interpretation of longitudinal cross-sectional profile B-B' of the Rukwa Rift (same as in Fig. 2d and S24d) highlighting the spatial
 723 relationships between the broad seismicity distribution, detected fluid-related clustered events (colored upper-mantle events), upper-crustal
 724 low-velocity anomalies, moho depth distribution, and the zoning of active deformation at the rift-tip.
 725
 726

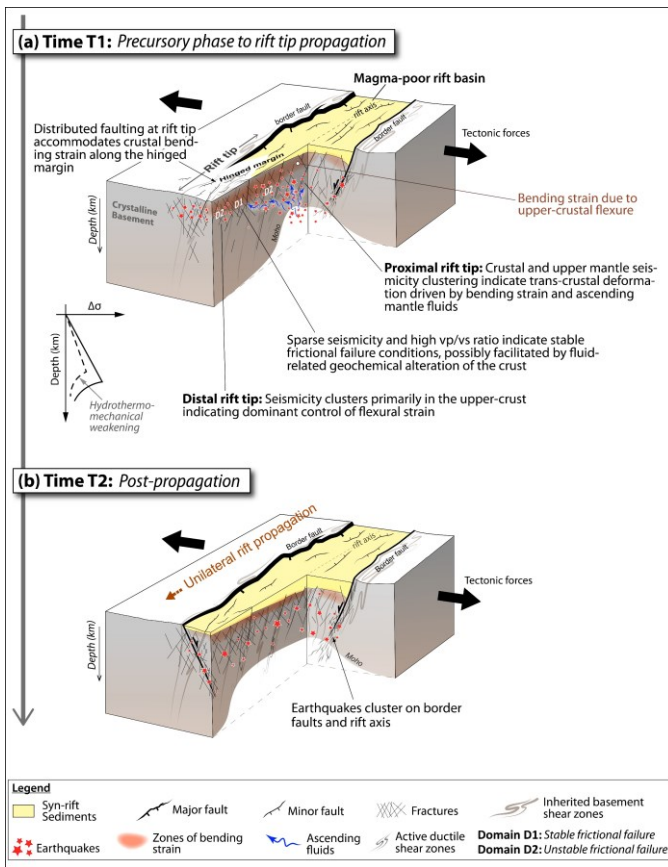


Figure 6. Cartoons showing the proposed model of crustal strain accommodation during the unilateral propagation phases of active continental rift tips, based on the results of our study. Note that the panel b of the cartoon is idealized to speculate a likelihood of decreased seismicity at a paleo-rift tip zone post propagation of the rift tip and does not include earthquakes occurrence due to other tectonic processes that may promote strain localization within the rift axis.

Formatted: Space Before: 12 pt, After: 12 pt, Line space: 1.5 lines

779 **Conclusions**

780 To understand how tectonic strain is accommodated along actively propagating magma-poor continental rifts, we constructed
781 three-dimensional velocity models of the crystalline crust beneath the Rukwa-Tanganyika Rift Zone. ~~where the Tanganyika~~
782 ~~Rift is interacting with the Rukwa and Mweru-Wantipa rifts.~~ The results show anomalously high Vp/Vs ratio anomalies at the
783 ~~current Rukwa and Mweru-Wantipa~~ rift tips and ~~their~~ rift interaction zones ~~with the Tanganyika Rift~~, representing, for the first
784 time, geophysical evidence demonstrating ~~that an initial~~ crustal softening of ~~the rift tip may be required to initiate~~ rift tips in a
785 ~~region of active~~ unilateral rift propagation. ~~We detect distinct earthquake families within the deeper rift-tip seismicity clusters~~
786 ~~that exhibit linear upward migration patterns, and temporal evolution patterns that suggest fluid migration and associated creep~~
787 ~~failure.~~ We determine that brittle damage due to bending ~~stresses and associated strain, potentially compounded and~~
788 ~~thermomechanical alteration of the crust~~ by ~~ascending fluids (mantle-sourced volatiles and hydrothermal fluids) are~~
789 ~~accommodating the mechanical~~ weakening at the rift ~~tip's flexural margin facilitates the observed pronounced softening. These~~
790 ~~new tip to facilitate the propagation of the rift tip into unrifted crust within the rift interaction zones. Furthermore, we observe~~
791 ~~a transition from collocated thinned crust and through-going crustal and upper-mantle seismicity in the proximal tip zones, to~~
792 ~~dominantly upper-crustal seismicity in the distal tip zones, indicating an along-axis variation in the controls on rift tip~~
793 ~~deformation. The results of this study provide new and compelling insight~~ insights into how continental rift tips propagate, link,
794 and coalesce to form continuous axial rift floors — a necessary ingredient for initiating large-scale continental break-up
795 ~~axis~~ axes.

796

797 **Acknowledgments**

798 This project was supported by funds from the Columbia Climate School ~~and the Vetlesen Foundation~~ awarded to Folarin
799 Kolawole. We thank Finnigan Illsley-Kemp, ~~Frank Zwaan, and anonymous reviewers~~ for comments that helped to improve
800 the earlier ~~version and later versions~~ of the manuscript. Some figures are plotted using GMT (Wessel et al., 2019).

801 **Author contributions**

802 F.K. and R.A. conceptualized the project. R.A. performed the modeling. F.K. and R.A. interpreted the results. F.K. wrote the
803 manuscript. R.A. revised the manuscript.

804 **Competing interests**

805 The authors declare no competing interests.

806 **Open Research**

807 Computer programs and files to reproduce our results are in Ajala and Kolawole (2023).

808

809

810

References

- Aanyu, K. and Koehn, D., 2011. Influence of pre-existing fabrics on fault kinematics and rift geometry of interacting segments: analogue models based on the Albertine Rift (Uganda), Western Branch-East African Rift System. *Journal of African Earth Sciences*, 59(2-3), pp.168-184.
- Acocella, Faccenna, Funicello and Rossetti, 1999. Sand-box modelling of basement-controlled transfer zones in extensional domains. *Terra Nova*, 11(4), pp.149-156.
- Ajala, R., and Kolawole, F. (2023). Reproducibility material for crustal softening at propagating rift tips. Retrieved from <https://doi.org/10.5281/zenodo.8302196>
- Ajala, R., Kolawole, F. and Menke, W., 2024. Blind magmatism abets nonvolcanic continental rifting. *Communications Earth & Environment*, 5(1), p.80.
- Ajala, R. and Persaud, P. (2021). Effect of Merging Multiscale Models on Seismic Wavefield Predictions Near the Southern San Andreas Fault. *Journal of Geophysical Research: Solid Earth*, 126, 1-23.
- Allam, A. A., Ben-Zion, Y., Kurzon, I., and Vernon, F., 2014. Seismic velocity structure in the Hot Springs and Trifurcation areas of the San Jacinto fault zone, California, from double-difference tomography. *Geophysical Journal International*, 198, 978-999.
- Allken, V., Huismans, R.S. and Thieulot, C., 2012. Factors controlling the mode of rift interaction in brittle-ductile coupled systems: A 3D numerical study. *Geochemistry, Geophysics, Geosystems*, 13(5).
- Blanpied, M.L., Lockner, D.A. and Byerlee, J.D., 1991. Fault stability inferred from granite sliding experiments at hydrothermal conditions. *Geophysical Research Letters*, 18(4), pp.609-612.
- Brune, S., Kolawole, F., Olive, J.A., Stamps, D.S., Buck, W.R., Buitter, S.J., Furman, T. and Shillington, D.J., 2023. Geodynamics of continental rift initiation and evolution. *Nature Reviews Earth & Environment*, 4(4), pp.235-253.
- Carpenter, B.M., Marone, C. and Saffer, D.M., 2011. Weakness of the San Andreas Fault revealed by samples from the active fault zone. *Nature Geoscience*, 4(4), pp.251-254.
- Celli, N. L., Lebedev, S., Schaeffer, A. J., and Gaina, C. (2020). African cratonic lithosphere carved by mantle plumes. *Nature Communications*, 11(92), 1-10.
- Chatterjee, S.N., Pitt, A.M. and Iyer, H.M., 1985. Vp/Vs ratios in the Yellowstone national park region, Wyoming. *Journal of Volcanology and Geothermal Research*, 26(3-4), pp.213-230.
- Chen, Y.L., Ni, J., Shao, W. and Azzam, R., 2012. Experimental study on the influence of temperature on the mechanical properties of granite under uni-axial compression and fatigue loading. *International Journal of Rock Mechanics and Mining Sciences*, 56, pp.62-66.
- Cormier, V. F. and Spudich. (1984). Amplification of ground motion and waveform complexity in fault zones: examples from the San Andreas and Calaveras Faults. *Geophys. J. R. astr. Soc.*, 79, 135-152.
- Corti, G., 2004. Centrifuge modelling of the influence of crustal fabrics on the development of transfer zones: insights into the mechanics of continental rifting architecture. *Tectonophysics*, 384(1-4), pp.191-208.
- Craig, T. J., Jackson, J. A., Priestley, K., and McKenzie, D. (2011). Earthquake distribution patterns in Africa: Their relationship to variations in lithospheric and geological structure, and their rheological implications. *Geophysical Journal International*, 185(1), 403-434. <https://doi.org/10.1111/j.1365-246X.2011.04950.x>
- Daly, M. C. (1988). *Crustal Shear Zones in Central Africa: a Kinematic Approach to Proterozoic Tectonics. Episodes 11 (1), 5-11. doi:10.18814/epiugs/1988/v11i1/003*
- Delvaux, D., 1989. The Karoo to recent rifting in the western branch of the East-African Rift System: a bibliographical synthesis. In: *Mus. Roy. Afr. Centr., Tervuren (Belg.), Dept. Geol. Min., Rapp. Ann. 1990, 1991*, pp. 63-83.
- Delvaux, D., and Barth, A. (2010). African stress pattern from formal inversion of focal mechanism data. *Tectonophysics*, 482(1-4), 105-128. <https://doi.org/10.1016/j.tecto.2009.05.009>.
- Delvaux, D., Kervyn, F., Macheyekki, A. S., and Temu, E. B. (2012). Geodynamic Significance of the TRM Segment in the East African Rift (W-Tanzania): Active Tectonics and Paleostress in the Ufipa Plateau and Rukwa basin. *J. Struct. Geology*, 37, 161-180.
- Fang, H., Yao, H., Zhang, H., Thurber, C., Ben-Zion, Y. and van der Hilst, R.D., 2019. V p/V s tomography in the southern California plate boundary region using body and surface wave travelttime data. *Geophysical Journal International*, 216(1), pp.609-620.

Formatted: Underline, Font color: Blue

- 861 Foster, A. N., and Jackson, J. A. (1998). Source parameters of large African earthquakes: Implications for crustal rheology
862 and regional kinematics. *Geophysical Journal International*, 134(2), 422–448. [https://doi.org/10.1046/j.1365-](https://doi.org/10.1046/j.1365-246x.1998.00568.x)
863 [246x.1998.00568.x](https://doi.org/10.1046/j.1365-246x.1998.00568.x)
- 864 Gaherty, J.B., Zheng, W., Shillington, D.J., Pritchard, M.E., Henderson, S.T., Chindandali, P.R.N., Mdala, H., Shuler, A.,
865 Lindsey, N., Oliva, S.J. and Nooner, S., 2019. Faulting processes during early-stage rifting: Seismic and geodetic
866 analysis of the 2009–2010 Northern Malawi earthquake sequence. *Geophysical Journal International*, 217(3),
867 pp.1767-1782.
- 868 Ganbat, A., Tsujimori, T., Boniface, N., Pastor-Galán, D., Aoki, S. and Aoki, K., 2021. Crustal evolution of the
869 Paleoproterozoic Ubendian Belt (SW Tanzania) western margin: a Central African Shield amalgamation tale.
870 *Gondwana Research*, 91, pp.286-306.
- 871 [Goebel, T. H. W., Rosson, Z., Brodsky, E. E., & Walter, J. I. \(2019\). Aftershock deficiency of induced earthquake sequences](#)
872 [during rapid mitigation efforts in Oklahoma. *Earth and Planetary Science Letters*, 522, 135-143.](#)
- 873 Goetze, C. and Evans, B., 1979. Stress and temperature in the bending lithosphere as constrained by experimental rock
874 mechanics. *Geophysical Journal International*, 59(3), pp.463-478.
- 875 Hanson, R.E., 2003. Proterozoic geochronology and tectonic evolution of southern Africa. Geological Society, London,
876 *Special Publications*, 206(1), pp.427-463.
- 877 Hauksson, E. and Unruh, J. (2007). Regional tectonics of the Coso geothermal area along the intracontinental plate boundary
878 in central eastern California: three-dimensional Vp and Vp/Vs models, spatio-temporal seismicity patterns, and
879 seismogenic deformation, *Journal of Geophysical Research*, 112(B6), 1-24.
- 880 Heilman, E., Kolawole, F., Atekwana, E. A., and Mayle, M. (2019). Controls of Basement Fabric on the Linkage of Rift
881 Segments. *Tectonics* 38 (4), 1337–1366. doi:10.1029/2018tc005362.
- 882 Hodgson, I., Illsley-Kemp, F., Gallacher, R., Keir, D., Ebinger, C. J., and Mtelela, K. (2017). Crustal Structure at a Young
883 Continental Rift: A Receiver Function Study from the Tanganyika Rift. *Tectonics*, 36, 1-17.
- 884 Hole, J. A. (1992). Nonlinear high-resolution three-dimensional seismic travel time tomography. *Journal of Geophysical*
885 *Research: Solid Earth*, 97(B5), 6553-6562. <http://dx.doi.org/10.1029/92JB00235>
- 886 Jones, D. J. R. (2020). A summary of the East Africa Rift Temperature and Heat flow Model (EARTH). British Geological
887 Survey Open Report, OR/20/006. 24pp.
- 888 Kolawole, F., Firkins, M.C., Al Wahaibi, T.S., Atekwana, E.A. and Soreghan, M.J., 2021a. Rift interaction zones and the
889 stages of rift linkage in active segmented continental rift systems. *Basin Research*, 33(6), pp.2984-3020.
- 890 Kolawole, F., Johnston, C.S., Morgan, C.B., Chang, J.C., Marfurt, K.J., Lockner, D.A., Reches, Z. and Carpenter, B.M., 2019.
891 The susceptibility of Oklahoma’s basement to seismic reactivation. *Nature Geoscience*, 12(10), pp.839-844.
- 892 Kolawole, F., Phillips, T.B., Atekwana, E.A. and Jackson, C.A.L., 2021b. Structural inheritance controls strain distribution
893 during early continental rifting, lukwa rift. *Frontiers in Earth Science*, 9, p.707869.
- 894 Kolawole, F., Vick, T., Atekwana, E.A., Laó-Dávila, D.A., Costa, A.G., and Carpenter, B.M. (2022). Strain Localization and
895 Migration During the Pulsed Lateral Propagation of the Shire Rift Zone, East Africa. *Tectonophysics*, 839, 229499.
896 Doi: 10.1016/j.tecto.2022.229499.
- 897 Kolawole, F., Xue, L. and Dulanya, Z., 2023. Rapid Versus Delayed Linkage and Coalescence of Propagating Rift Tips.
898 *Authorea Preprints*, 10.22541/essoar.168167202.29986035/v1.
- 899 Kranz, R. L. (1979). Crack-crack and crack-pore interactions in stressed granite. *International Journal of Rock Mechanics and*
900 *Mining Sciences and Geomechanics Abstracts*, 16(1), 37–47.
- 901 Lavayssière, A., Drooff, C., Ebinger, C. J., Gallacher, R., Illsley-Kemp, F., Oliva, S. J., and Keir, D. (2019). Depth Extent and
902 Kinematics of Faulting in the Southern Tanganyika Rift, Africa. *Tectonics*, 38, 842-862.
- 903 Lemna, O. S., Stephenson, R., and Cornwell, D. G. (2019). The Role of Pre-existing Precambrian Structures in the
904 Development of Rukwa Rift Basin, Southwest Tanzania. *J. Afr. Earth Sci.* 150, 607–625.
905 doi:10.1016/j.jafrearsci.2018.09.015.
- 906 Le Pourhiet, L., Chamot-Rooke, N., Delescluse, M., May, D.A., Watremez, L. and Pubellier, M., 2018. Continental break-up
907 of the South China Sea stalled by far-field compression. *Nature Geoscience*, 11(8), pp.605-609.
- 908 Molnar, N.E., Cruden, A.R. and Betts, P.G., 2019. Interactions between propagating rifts and linear weaknesses in the lower
909 crust. *Geosphere*, 15(5), pp.1617-1640.

- 910 Morley, C. K., Cunningham, S. M., Harper, R. M., and Wescott, W. A. (1992). Geology and Geophysics of the Rukwa Rift,
 911 East Africa. *Tectonics* 11 (1), 69–81. doi:10.1029/91tc02102.
- 912 Morley, C. K., Wescott, W. A., Harper, R. M., and Cunningham, S. M. (1999). Geology and Geophysics of the Rukwa Rift.
 913 *Geoscience of Rift Systems-Evolution of East Africa*. AAPG Stud. Geology. 44, 91–110.
- 914 Muirhead, J. D., Wright, L. J., and Scholz, C. A. (2019). Rift evolution in regions of low magma input in East Africa. *Earth
 915 and Planetary Science Letters*, 506, 332–346.
- 916 Mulaya, E., Gluyas, J., McCaffrey, K., Phillips, T. and Ballentine, C. (2022). Structural geometry and evolution of the Rukwa
 917 Rift Basin, Tanzania: Implications for helium potential. *Basin Research* 34, 938-960.
- 918 [Nakajima, J., Matsuzawa, T., Hasegawa, A. and Zhao, D., 2001. Three-dimensional structure of Vp, Vs, and Vp/Vs beneath
 919 northeastern Japan: Implications for arc magmatism and fluids. *Journal of Geophysical Research: Solid Earth*,
 920 106\(B10\), pp.21843-21857.](#)
- 921 Nelson, R.A., Patton, T.L. and Morley, C.K., 1992. Rift-segment interaction and its relation to hydrocarbon exploration in
 922 continental rift systems. *AAPG bulletin*, 76(8), pp.1153-1169.
- 923 Neuharth, D., Brune, S., Glerum, A., Heine, C. and Welford, J.K., 2021. Formation of continental microplates through rift
 924 linkage: Numerical modeling and its application to the Flemish Cap and Sao Paulo Plateau. *Geochemistry,
 925 Geophysics, Geosystems*, 22(4), p.e2020GC009615.
- 926 Njinju, E.A., Atekwana, E.A., Stamps, D.S., Abdelsalam, M.G., Atekwana, E.A., Mickus, K.L., Fishwick, S., Kolawole, F.,
 927 Rajaonarison, T.A. and Nyalugwe, V.N., 2019. Lithospheric structure of the Malawi Rift: Implications for magma-
 928 poor rifting processes. *Tectonics*, 38(11), pp.3835-3853.
- 929 Nunn, J.A., 1985. State of stress in the northern Gulf Coast. *Geology*, 13(6), pp.429-432.
- 930 Olson, J.E., 2004. Predicting fracture swarms—The influence of subcritical crack growth and the crack-tip process zone on
 931 joint spacing in rock. *Geological Society, London, Special Publications*, 231(1), pp.73-88.
- 932 Pérez-Gussinyé, M., Collier, J.S., Armitage, J.J., Hopper, J.R., Sun, Z. and Ranero, C.R., 2023. Towards a process-based
 933 understanding of rifted continental margins. *Nature Reviews Earth & Environment*, 4(3), pp.166-184.
- 934 [Raggiunti, M., Keir, D., Pagli, C., & Lavayssière, A. \(2023\). Evidence of Fluid Induced Earthquake Swarms From High
 935 Resolution Earthquake Relocation in the Main Ethiopian Rift. *Geochemistry, Geophysics, Geosystems*, 24, 1-16.](#)
- 936 [Reasenbergh, P. \(1985\). Second-Order Moment of Central California Seismicity, 1969-1982. *Journal of Geophysical Research*,
 937 90\(87\), 5479-5495.](#)
- 938 Roberts, E. M., Stevens, N. J., O'Connor, P. M., Dirks, P. H. G. M., Gottfried, M. D., Clyde, W. C., Armstrong, R. A., Kemp,
 939 A. I. S., and Hemming, S. (2012). Initiation of the western branch of the East African Rift coeval with the eastern
 940 branch. *Nature Geoscience*, 5(4), 289–294. <https://doi.org/10.1038/ngeo1432><https://doi.org/10.1038/ngeo1432>.
- 941 [Roland, M., & McGuire, J. J. \(2009\). Earthquake swarms on transform faults. *Geophysical Journal International*, 178, 1677-
 942 1690.](#)
- 943 [Saeidi, H., Hansen, S.E., Nyblade, A.A. and Haag, R., 2024. Mantle structure beneath the Damara Belt in south-central Africa
 944 imaged using adaptively parameterized P-wave tomography. *Journal of Geophysical Research: Solid Earth*, 129\(3\),
 945 p.e2023JB027965.](#)
- 946 Shaban, S., Scholz, C.A., Kolawole, F. (2023). The Deep Basin and Underlying Basement Structure of the Tanganyika Rift.
 947 *Tectonics*, 42, e2022TC007726.
- 948 Stamps, D. S., Calais, E., Saria, E., Hartnady, C., Nocquet, J. M., Ebinger, C. J., and Fernandes, R. M. (2008). A kinematic
 949 model for the East African Rift. *Geophysical Research Letters*, 35(5).
- 950 Stein, S., Sleep, N.H., Geller, R.J., Wang, S.C. and Kroeger, G.C., 1979. Earthquakes along the passive margin of eastern
 951 Canada. *Geophysical Research Letters*, 6(7), pp.537-540.
- 952 Stevens, V.L., Sloan, R.A., Chindandali, P.R., Wedmore, L.N., Salomon, G.W., Muir, R.A., 2021. The entire crust can be
 953 seismogenic: evidence from Southern Malawi. *Tectonics* 40 (6). <https://doi.org/10.1029/2020TC006654>
 954 e2020TC006654.
- 955 Tiercelin, J.J., Pflumio, C., Castrec, M., Boulégué, J., Gente, P., Rolet, J., Coussemont, C., Stetter, K.O., Huber, R., Buku, S.
 956 and Mifundu, W., 1993. Hydrothermal vents in Lake Tanganyika, East African, Rift system. *Geology*, 21(6), pp.499-
 957 502.

Formatted: French (France)

958 Van Herwaarden, D., Thrastarson, S., Halpa, V., Afanasiev, M., Trampert, J., and Fichtner, A. (2022). Full-Waveform
959 Tomography of the African Plate Using Dynamic Mini-Batches. *Journal of Geophysical Research: Solid Earth*, 126,
960 1-22.

961 Van Wijk, J.K., Blackman, D.K., 2005. Dynamics of continental rift propagation: the endmember modes. *Earth Planet. Sci.*
962 *Lett.* 229 (3–4), 247–258.

963 Veatch, A. C. (1935). Evolution of the Congo Basin. *GSA Memoir* 3.

964 Versfelt, J., and Rosendahl, B. (1989). Relationship between pre-rift structure and rift architecture in Lakes Tanganyika and
965 Malawi, East Africa. *Nature*, 337, 354–357.

966 Vidale, J. E. (1990). Finite-difference calculation of traveltimes in three dimensions. *Geophysics*, 55(5), 521-526.

967 Wessel, P., Luis, J. F., Uieda, L., Scharroo, R., Wobbe, F., Smith, W. H. F., and Tian, D. (2019). The generic mapping tools
968 version 6. *Geochemistry, Geophysics, Geosystems*, 20, 1-20. <https://doi.org/10.1029/2019gc008515>

969 Yang, Z., and Chen, W. P. (2010). Earthquakes along the East African Rift System: A multiscale, system-wide perspective.
970 *Journal of Geophysical Research*, 115, B12309.
971 <https://doi.org/10.1029/2009JB006779><https://doi.org/10.1029/2009JB006779>

972 [Zaliapin, I., & Ben-Zion, Y. \(2013\). Earthquake clusters in southern California I: Identification and stability. *Journal of*](#)
973 [Geophysical Research: Solid Earth](#), 118, 2847-2864.

974 [Zaliapin, I., Gabrielov, A., Keilis-Borok, V., & Wong, H. \(2008\). Clustering Analysis of Seismicity and Aftershock](#)
975 [Identification. *Physical Review Letters*, 101, 1-4.](#)

976 [Zhang, Q., & Shearer, P. \(2016\). A new method to identify earthquake swarms applied to seismicity near the San Jacinto Fault,](#)
977 [California. *Geophysical Journal International*, 205, 995-1005.](#)

978 Zheng, W., Oliva, S.J., Ebinger, C. and Pritchard, M.E., 2020. Aseismic deformation during the 2014 M w 5.2 Karonga
979 earthquake, Malawi, from satellite interferometry and earthquake source mechanisms. *Geophysical Research Letters*,
980 47(22), p.e2020GL090930.

981 Zwaan, F., and Schreurs, G. (2020). Rift segment interaction in orthogonal and rotational extension experiments: Implications
982 for the large-scale development of rift systems. *Journal of Structural Geology*, 140, 104119.
983 <https://doi.org/10.1016/j.jsg.2020.104119>

984 Zwaan, F., Schreurs, G., Naliboff, J., and Buitter, S. J. (2016). Insights into the effects of oblique extension on continental rift
985 interaction from 3D analogue and numerical models. *Tectonophysics*, 693, 239–260.
986 <https://doi.org/10.1016/j.tecto.2016.02.036>